



Longitudinal, label-free, high-resolution imaging of glioblastoma spheroid response to therapy: a translational tool for preclinical evaluation of chemotherapy, radiation, and immunotherapy

CAROLINE E. SERAFINI,^{1,2,†} AMIN DAVARZANI,^{3,4,†} DAN CAPPABIANCA,^{5,6} ZHENMIN LI,⁷ DANIELA BAEZ COLLAZOS,² DENIZ MAMAGHANI,³ LEIDONG MAO,^{3,4} KRISHANU SAHA,^{5,6} LOHITASH KARUMBAIAH,^{3,8,9,10} AND FRANCISCO E. ROBLES^{1,2,7,*}

¹George W. Woodruff School of Mechanical Engineering, Georgia Institute of Technology, 801 Ferst Drive NW, Atlanta, Georgia 30318, USA

²The Wallace H. Coulter Department of Biomedical Engineering, Georgia Institute of Technology, 313 Ferst Drive NW, Atlanta, Georgia 30332, USA

³Regenerative Bioscience Center, University of Georgia, 425 River Road, Athens, Georgia 30602, USA

⁴School of Electrical and Computer Engineering, University of Georgia, 200 D.W. Brooks Drive, Athens, Georgia 30602, USA

⁵Department of Biomedical Engineering, University of Wisconsin Madison, 330 N. Orchard Street, Madison, Wisconsin 53715, USA

⁶Wisconsin Institutes for Discovery, University of Wisconsin Madison, 330 North Orchard Street, Madison, Wisconsin 53715, USA

⁷School of Electrical and Computer Engineering, Georgia Institute of Technology, 777 Atlantic Drive NW, Atlanta, Georgia 30332, USA

⁸Department of Animal and Dairy Science, University of Georgia, 425 River Road, Athens, Georgia 30602, USA

⁹College of Agricultural and Environmental Sciences, University of Georgia, 147 Cedar Street, Athens, Georgia 30602, USA

¹⁰Division of Neuroscience, Biomedical and Translational Sciences Institute, University of Georgia, 105 Foster Road, Athens, Georgia 30602, USA

*These authors contributed equally to this work.

*robles@gatech.edu

Received 28 July 2025; revised 9 December 2025; accepted 10 December 2025; published 27 January 2026

Glioblastoma (GBM) is an aggressive brain tumor with limited treatment options and poor patient survival, underscoring the need for novel, to our knowledge, therapeutic strategies and improved preclinical models. Patient-derived tumor spheroids (PDTSSs) offer a physiologically relevant *in vitro* platform for evaluating treatments such as chimeric antigen receptor (CAR) T cell therapy, chemotherapy, and radiation. However, significant challenges remain in monitoring the complex three-dimensional (3D) microenvironment of the GBM PDTSSs. Current imaging techniques used for this purpose are primarily endpoint analyses which lack critical real-time, non-invasive capabilities that ultimately preclude longitudinal and continuous monitoring. In this study, we introduce quantitative oblique back-illumination microscopy (qOBM) as a label-free and non-invasive imaging approach for longitudinal and continuous, high-resolution monitoring of GBM PDTSSs during treatment. qOBM enables real-time visualization of cellular processes, including apoptosis, cell migration, and T cell-mediated cytotoxicity by leveraging tomographic refractive index-based quantitative imaging. We construct a compact qOBM system that fits within common incubators and apply it to study the effects of radiation, chemotherapy, and immunotherapy on three patient-derived GBM cell lines, extracting both static and dynamic image features over a 72 h treatment period. Additionally, we develop machine learning models to predict spheroid viability and cytotoxicity, demonstrating the potential of qOBM to enhance treatment evaluation. Our findings establish qOBM as a powerful tool for longitudinal and continuous spheroid monitoring, offering a non-destructive, high-resolution alternative to conventional endpoint assays and improving the evaluation of preclinical treatments for GBM. © 2026 Optica Publishing Group under the terms of the [Optica Open Access Publishing Agreement](#)

<https://doi.org/10.1364/OPTICA.574860>

1. INTRODUCTION

Glioblastoma (GBM) is a devastating disease with a poor prognosis that has motivated the development of both improved preclinical models and novel therapeutic approaches [1]. One of the most promising emerging preclinical models involves growing excised primary tumor cells in three-dimensional cultures called patient-derived tumor spheroids (PDTSSs) [2–14]. These

cultures incorporate both tumor and surrounding cells, closely replicating individual patient's tumor microenvironment, cellular diversity, and genetic mutations. As a result, PDTSSs offer a more accurate representation of human disease than traditional 2D cell cultures or animal models [2–17]. With respect to therapeutic approaches, in addition to chemotherapy and radiation, chimeric antigen receptor (CAR) T cell therapy has emerged as a promising immunotherapy strategy to treat GBM. This therapy involves

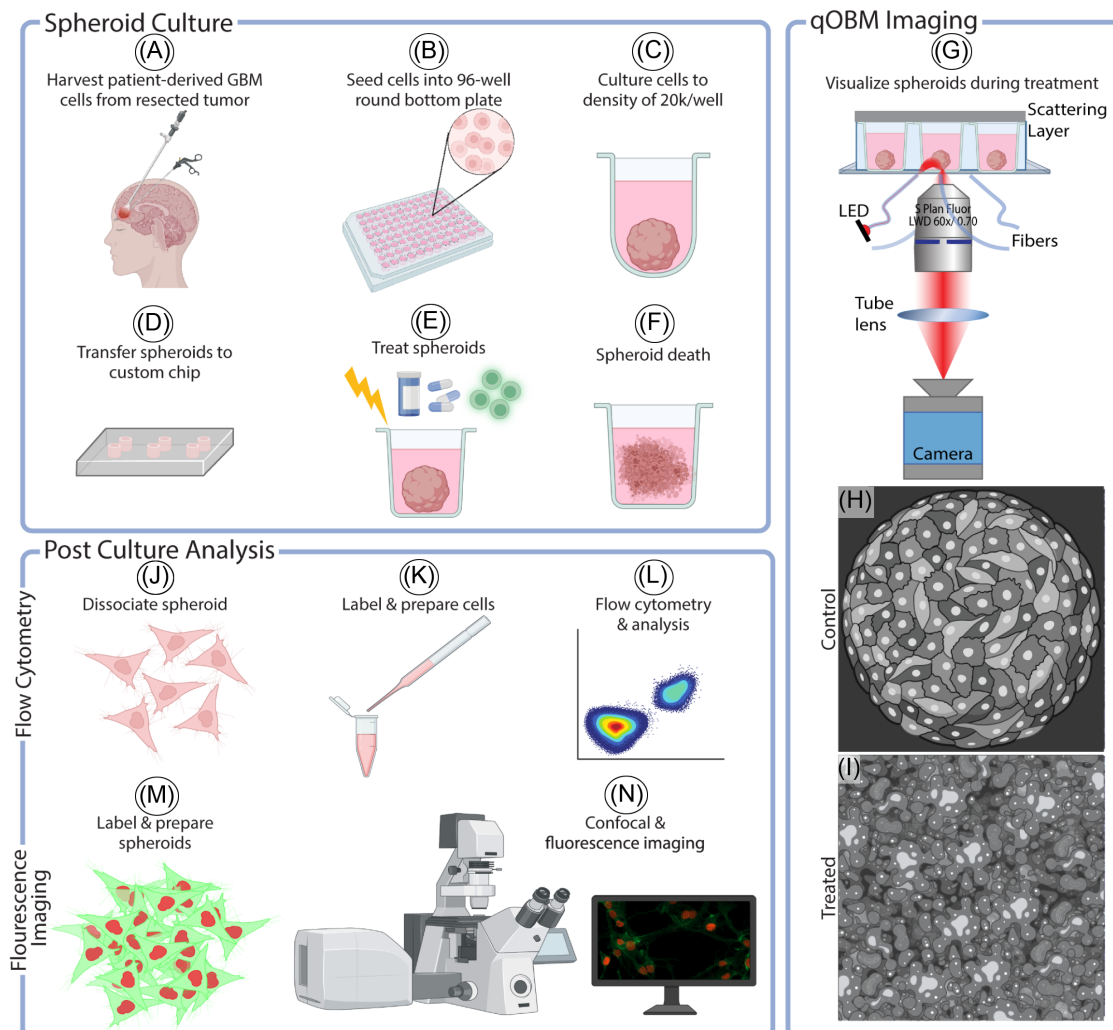


Fig. 1. qOBM overview/process overview: (A)–(F) show spheroid formation. This includes (A) harvesting cells from a patient, (B) seeding said cells in a round-bottom well plate for spheroid formation, (C) growing the cells and spheroids to a large enough size, and (D) transferring the spheroids to a custom chip. Upon placement in the chip, (E) spheroids are then treated with radiation, chemotherapy, and immunotherapy. In response to treatment, (F) we can see spheroid death and morphologic changes. (G) shows how qOBM can be integrated for continuous, non-invasive imaging and spheroid monitoring during treatment. (H)–(I) show illustrations of qOBM images of a (H) control spheroid and a (I) treated, dead spheroid. Finally, (J)–(N) show the typical post-processing of spheroids. (J)–(L) outline flow cytometry of spheroids where (J) the spheroid is removed from the chip and disassociated, (K) labeled, and (L) imaged and analyzed with flow cytometry. (M) and (N) show fluorescence microscopy (like confocal imaging) where (M) the spheroid is prepared and labeled to (N) be imaged.

genetically engineering T cells to express synthetic receptors that selectively target tumor-associated antigens [18]. However, the efficacy of CAR-T cell therapy in GBM (and solid tumors in general) has been limited and requires further development [19]. Again, spheroid models serve as a valuable platform to study and improve CAR-T cell therapy, as visualized in Figs. 1A–1F.

Despite advances in spheroid culture, effective monitoring of treatment response in physiologically relevant GBM models remains challenging due to a lack of high-resolution imaging tools that can be applied non-invasively and longitudinally. The gold standard for gaining insight into spheroid culture is flow cytometry. As shown in Figs. 1J–1L, spheroids are disassociated, labeled, and then analyzed to assess genotypic expression. While this provides rich molecular information, this is an endpoint analysis and is not able to capture structure nor dynamic changes in function longitudinally. To analyze spheroids without labels, non-destructively, and longitudinally, brightfield microscopy is commonly employed

to provide information about spheroid shape and size throughout the duration of cell culture; [20] however, brightfield imaging of thick structures lacks cellular and subcellular detail. To gain access to (sub)cellular information, other imaging modalities have been employed, including fluorescence-based imaging (as shown in Figs. 1M and 1N) [21,22], light-sheet imaging [23], and immunohistochemistry (IHC) staining [24–26]. These methods can provide (sub)cellular details, but they are also primarily endpoint measurements that do not facilitate non-invasive, *in vitro* imaging of spheroids longitudinally and continuously.

In this study, we present quantitative oblique back-illumination microscopy (qOBM) as a novel, cost-effective approach to monitor GBM spheroids longitudinally, continuously, and non-invasively, in real-time, and with subcellular-resolution, as seen in Figs. 1G–1I. qOBM is a quantitative phase imaging (QPI) method that delivers label-free, high-contrast, quantitative information

of cellular and subcellular structures based on endogenous refractive index (RI) properties (which are directly proportional to dry mass) [27–29]. However, unlike traditional QPI methods, qOBM uniquely enables real-time tomographic imaging of thick scattering tissues, including spheroids [27–29]. Further, qOBM can provide functional information by monitoring fast dynamic changes in RI (effectively, mass transport) [30].

Using a bench-top and compact qOBM system that can be placed inside commonly used cell culture incubators, we study three unique patient-derived GBM cell lines with clinically relevant mutations exposed to (1) radiation, (2) temozolomide (TMZ) chemotherapy, (3) an experimental glycosaminoglycan antagonist—Surfen, and (4) targeted and non-targeted T cell immunotherapy. The results show unique behaviors, including targeted T cells attacking cancer cells in real-time, T cells rapidly traversing through the spheroid, cellular mitosis, and cellular apoptosis among other complex processes. Leveraging the quantitative RI images produced by qOBM, we extract static and dynamic image features from the spheroids over the course of treatment (72 h), and develop machine learning models to predict spheroid cytotoxicity and viability. These results demonstrate qOBM as an invaluable tool for longitudinal, continuous, non-destructive spheroid monitoring with the ability to predict treatment effectiveness. The approach presented here not only significantly enhances—and in some cases supplants—end-point analyses, but also paves the way for novel avenues of inquiry of unperturbed *in vitro* 3D cell cultures.

2. RESULTS

A. qOBM Imaging Provides Unique Insight into Immunotherapy-Treated Spheroids and Predicts Treatment-Mediated Cytotoxicity

We first analyze the general structure and dynamics of a control spheroid with no treatment, a spheroid co-cultured with untargeted (no CAR) T cells, and a spheroid co-cultured with targeted CAR-T cells (see Section 4 for details). The co-cultures take place in a custom culture insert as depicted in Fig. 1D and described in more detail in *Supplement 1*, Section 1. As seen in Figs. 2A–2D, qOBM allows for visualization of the GBM spheroid and CAR-T cell co-culture in a manner closely resembling traditional images obtained with confocal microscopy techniques (but in gray scale). Here, the confocal images (from separate samples) are labeled with DAPI (blue) to visualize nuclei, AF488 (green) to visualize polymerized actin, the anti-CAR antibody (red) to visualize CAR-T cells, and anti-granzyme B antibody (orange) to visualize granzyme B accumulation. Note granzyme B is used to label cytotoxic cells as a result of T cell induced cell death [31]. Figures 2A and 2B show a Day 0 spheroid where CAR-T cells have just been added to the culture. Here, we see a lack of granzyme B polarization at the CAR-T cell/GBM interface. Figures 2C and 2D show the co-cultures after 3 days. In Fig. 2C, we see granzyme B accumulation at the CAR-T cell/GBM contact site on Day 3 (indicated by red arrows), indicating immune synapse formation and cytotoxic granule polarization. While qOBM does not provide the molecular specificity to detect cytotoxic granule polarization, we do see high RI granule formation within the CAR-T cells, which is indicative of cell death using qOBM (more on this below) and likely corresponds to granzyme B. A zoomed-in region of cell death can be seen in the inset of Fig. 2D.

A distinct and significant advantage of qOBM over fluorescence microscopy and other methods of analyzing spheroids is the ability to perform continuous and longitudinal, non-invasive imaging, which uniquely enables qOBM to visualize, for example, T cell infiltration and killing of GBM cells. To study the movement of targeted CAR-T cells and untargeted T cells, we imaged the co-cultures daily for 3 days, taking a qOBM image every 10 s for 30 min each day. Using these time-lapse videos, we observe previously unseen phenomena of T cells attacking 3D spheroid (Figs. 2E and 2F, indicated by red arrows) and the T cells traversing through the spheroid (Figs. 2G and 2H, indicated by blue arrows), both of which occur in a timescale of seconds. These stills can be further visualized in [Visualization 1](#), [Visualization 2](#), [Visualization 3](#) and [Visualization 4](#).

With the ability to visualize T cell activity, we then sought to characterize the movement of the CAR and untargeted T cells in the culture. As seen in Figs. 2K and 2L and [Visualization 5](#) and [Visualization 6](#), we can track the movement of individual T cells throughout the spheroids. We see that in the spheroids treated with CAR-T cells, the immune cells appear to move through the spheroid with more complex and tortuous paths. Further, we see different functionalities of the T cells with some of the stationary CAR-T cells attacking the spheroid, while others move quickly through the spheroid. In comparison, untargeted T cells appeared to move more slowly. To quantify the differences in movement between the CAR and untargeted T cells, we utilized the time-and-spatially resolved T cell paths to calculate T cell speed and path complexity as determined by the time-dependent Yaghoobi fractal dimension [32]. As seen in Figs. 2I and 2J, both of these values were determined to be statistically significantly different between the CAR- and untargeted T cells ($P = 0.0002$ and $P < 0.0001$ for speed and fractal dimension, respectively), indicating that indeed the CAR-T cells move through the GBM spheroids with increased speed and path complexity compared to the untargeted T cells. Further, we plot histograms of these values in Figs. 2M and 2N. Here we can observe that while some of the CAR-T cells move with similar speed as the untargeted T cells, there are CAR-T cells on both ends of the spectrum that move much more quickly or have very slow speeds relative to the untargeted T cells. The slower CAR-T cells correspond to those that are actively attacking GBM cells and thus remain largely in place as they target a particular malignant cell. On the other hand, a different population of CAR-T cells moves quickly through the spheroids, potentially trying to quickly identify their next target. These differences may indicate different T cell expressions and/or activation state (i.e., phenotypes). Similarly, the histogram of fractal values shows many CAR-T cells exhibiting similar levels of path complexity similar to those of the untargeted T cells; however, a subset shows a behavior that is significantly skewed right, indicating a number of cells with far more complex patterns of movement.

The longitudinal imaging capabilities of qOBM, coupled with its rich cellular and subcellular contrast, also enable evaluation of treatment efficacy longitudinally. As demonstrated in Figs. 2O–2R, in Days 0–3 of the untargeted T cell group, we see well-rounded cells with well-defined nuclei. In contrast, the spheroid treated with CAR-T cells (Figs. 2S–2V) shows high levels of cell death, as indicated by high RI material, cell debris, nuclear fragmentation, and lack of clear, organized cell structure. These features underscore a clear

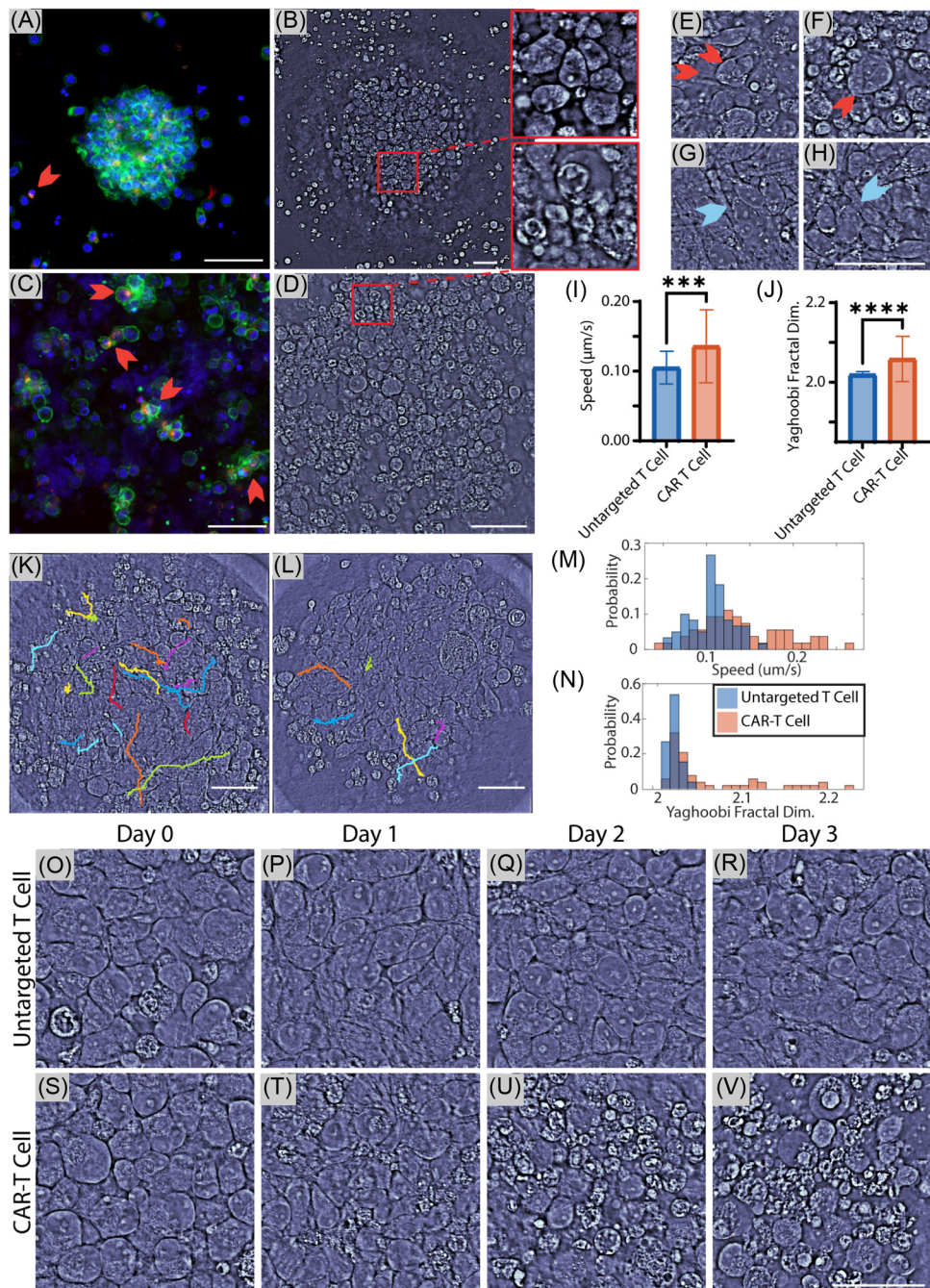


Fig. 2. Visual differences in immunotherapy-treated spheroids. (A)–(D) show a comparison of the confocal microscopy imaged (A), (C) with the qOBM imaged (B), (D) spheroids treated with immunotherapy. In the confocal images, nuclei are stained with DAPI (405 nm), actin with AF488 (488 nm), granzyme B with PE/Cy7 (561 nm), and CAR with APC (639 nm). Subsets are included of the qOBM images in B&D. (E)–(H) are accompanying images to [Visualization 1](#), [Visualization 2](#), [Visualization 3](#) and [Visualization 4](#) showing immunotherapy attacks (indicated by red arrows) on spheroid cells (E), (F) and T cells (indicated by blue arrows) traversing through the spheroid (G), (H). (K), (L) show the paths of tracked T cells for CAR-T cells (K) and untargeted T cells (L). These still images accompany [Visualization 5](#) and [Visualization 6](#). (I) compares the speed of T cells moving in the spheroid. (J) compares the Yaghoobi fractal dimension of the T cells moving in the spheroid. (M) shows a histogram of the T cell speed. (N) shows a histogram of the T cell Yaghoobi fractal value. (O)–(R) show two spheroids undergoing different courses of treatment over 3 days. (O)–(R) show a spheroid treated with untargeted T cells. (S)–(V) show a spheroid treated with CAR-T cells. All scale bars are 50 μm . (A)–(D) and (O)–(V) are from cell line N0830, (E)–(H) and (K)–(L) are from cell line N12159. (I), (J) and (M), (N) show values across all cell lines.

visual difference between the effects of untargeted and CAR-T cell-treated spheroids for GBM. For additional visualization, [Visualization 7](#), [Visualization 8](#), [Visualization 9](#), [Visualization 10](#), [Visualization 11](#), and [Visualization 12](#) show Z-stacks of the 3D spheroids with 1 μm Z-steps. These videos start at the

bottom of the spheroid and move up until contrast is lost (~150 μm deep). This is seen for control (no treatment) (20 \times : [Visualization 7](#), 60 \times : [Visualization 8](#)), untargeted T cell treated (20 \times : [Visualization 9](#), 60 \times : [Visualization 10](#)), and CAR-T cell treated (20 \times : [Visualization 11](#), 60 \times : [Visualization 12](#))

spheroids. The spheroids measured, on average, 0.9 mm in diameter ($\mu = 881 \mu\text{m}$, $\sigma = 141 \mu\text{m}$, $N = 14$), thus the 20× objective was able to capture an entire cross-sectional spheroid (20× field of view = 950 μm).

B. Incubator-Compatible Compact qOBM System Enables Continuous 72 h Spheroid Imaging

The data presented above were acquired using a bench-top microscope qOBM system (see Section 4.F), which could be coupled with a specialized sample-stage that includes temperature and gas-exchange control (i.e., a microscope stage incubator) to maintain near-physiological conditions during longitudinal experiments. However, such an approach tends to be bulky, complex, expensive, and can have limited utility. In this section, we present an

alternative and more universal approach for continuous, longitudinal imaging, where we leverage the simplicity of qOBM to develop a compact system that can fit within typical incubators used ubiquitously in biological, biomedical, and pharmaceutical labs. The compact system (described in Section 4.G)—shown in Fig. 3A inside an incubator—has a footprint of 8 × 12 × 10 in, includes automated XYZ scanning, and is controlled by an exterior computer, which eliminates the need to open the incubator or perturb the sample. The system is also low-cost (see Supplement 1, Table S1).

We demonstrate the ability of the miniaturized, incubator-compatible qOBM system to continuously and longitudinally monitor the spheroid by imaging a GBM spheroid treated with targeted CAR-T cells inside the incubator over a treatment

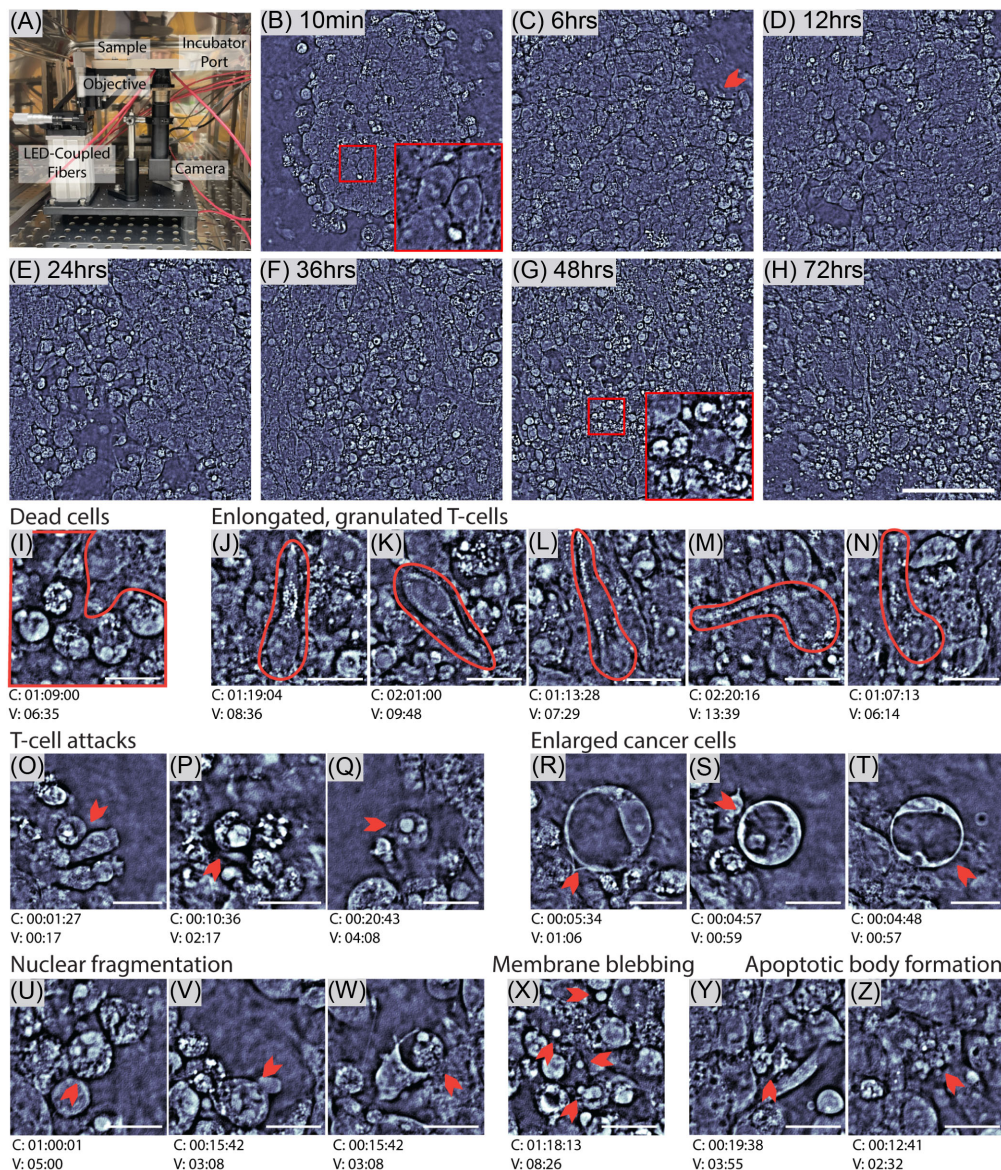


Fig. 3. Incubator-compatible compact qOBM system for continuous spheroid monitoring. (A) The qOBM system inside of the incubator. (B)–(H) Still images of the organoid treated with CAR-T therapy and monitored continuously for 3 days. (I)–(Z) Still images of particular dynamic processes occurring within the video. These processes include: dead GBM cells (I), elongated T cells with granules formed within the T cell (J)–(N), T cells attacking GBM cells (O)–(Q), enlarged GBM cells (R)–(T), GBM cells exhibiting nuclear fragmentation (U)–(W), GBM cells with membrane blebbing (X), and GBM cells with apoptotic body formation (Y), (Z). Scale bar for (B)–(H) is 100 μm . Scale bar for (I)–(Z) is 20 μm . All images are from the patient-derived GBM cell line N12159. Time stamps indicated in (I)–(Z) show the time stamp of the image in terms of co-culture time (C, Days:Hours:Minutes) and the time stamp in corresponding [Visualization 13](#) (V, Minutes:Seconds).

course of 3 days, with imaging acquisition every 10 s. As seen in Figs. 3B–3H, the structure of the spheroid clearly changes over the course of treatment. For example in Fig. 3B, the cross section of the spheroid appears fairly circular, with the GBM cells within showing round cells with well-defined nuclei as seen in the inset. As treatment progresses, we see T cells infiltrating the spheroid. Some areas, such as those indicated by the arrow in the top right corner of Fig. 3C, seem to recruit additional T cell clusters. Over the course of a few hours, the shape of the spheroid begins to collapse, losing its circular shape. This is potentially indicative of cytoskeletal changes in the spheroid structure. By hour 12 (Fig. 3D), we observe complete loss of spheroid shape and a high density of dead cells accumulating in the center of the spheroid. After 24 h, we begin to see a large amount of cell death (as seen in the high refractive index content in Fig. 3E). This cell death continues to increase over the next 48 h as seen in Figs. 3F–3H. An example of dead cells is seen in the inset in Fig. 3G.

The dynamics of complex interaction between the spheroid and CAR-T cells are better appreciated in video format in [Visualization 13](#). To highlight some of the features seen in the video, still images of dynamic processes are highlighted in Figs. 3I–3Z (the figures note the time in culture as well as the video time-stamp, for reference). These features include dead GBM cells (I), elongated T cells with granules formed within (J–N), T cells attacking GBM cells (O–Q), enlarged GBM cells (**R–T**), GBM cells exhibiting nuclear fragmentation (U–W), GBM cells with membrane blebbing (X), and GBM cells with apoptotic body formation (Y and Z). We showcase these examples to provide an idea of some of the features exhibited in [Visualization 13](#), but we stress that these examples only capture a small fraction of all of the biological events and observed features recorded during the 3 days of spheroid immunotherapy treatment.

This section demonstrates that the incubator-compatible qOBM system is able to provide unprecedented continuous and longitudinal access to the cellular and subcellular structure of GBM spheroid and co-cultured T cells in a manner that does not perturb the co-culture with the physiological conditions enabled by a common incubator.

C. Quantification of T Cell Cytotoxicity with qOBM

Next, we compare quantitative image features obtained with qOBM to the gold standard of flow cytometry, and develop an image-based assay for cytotoxicity. First, we determined the viability of cells in the spheroids using flow cytometry: Figs. 4D–4F show results of the average treatment-mediated cytotoxicity for a control group (no treatment), and untargeted T cell and targeted CAR-T cell treatment groups, for three distinct patient-derived GBM cell lines (N0830, N12159, and N12115), measured daily from Days 0 to 3. (The averages were taken from six replicates for each treatment type, PDTs, and time-point.) For the control group, cell viability levels remain constant during the 3 days of monitoring, as expected. For the immunotherapy-treated GBM spheroids, we see CAR-T cell-induced cytotoxicity increase over the course of treatment. Further, we see that the cytotoxic effect of CAR-T cell treatment is for the most part significantly higher than that of the untreated T cell group. Interestingly, we see the CAR-T cell treatment is more effective for two of the patient cell lines (N0830 and N12159), but is less so for patient cell line N12115. This may indicate that the CAR-T cell treatment is less potent against this particular patient's tumor cells compared to the others.

Following the flow cytometry analysis, we then identify qOBM image-based features that correlate with spheroid viability. We note that qOBM images are effectively a map of RI properties of the sample and RI is proportional to dry mass. A list of the extracted image features is described in Section 4.I. As seen in Fig. 4A, there is a strong correlation between a number of qOBM image features and the flow cytometry determined viability values—some of the most significant features included the standard deviation of phase values across an image ($R^2 = 0.59$), the entropy of the Laplacian transform of the image ($R^2 = 0.73$), and the entropy of the image ($R^2 = 0.78$). These values point to the idea that as spheroids experience increased cell death (higher cytotoxicity), the texture of qOBM images (i.e., disorganization of the RI/dry mass) increases as well. This can be seen in Figs. 1, 2, and 3, where there is a greater variety of high RI values within the images with treated spheroids. Figure 4A shows a clustergram of the subset of image features that correlate with the flow cytometry-measured cytotoxicity.

Using the 11 image features shown in Fig. 4A, we created a predictive linear regression model to serve as a image-based cytotoxicity assay (see Section 4.J). The results, shown in Fig. 4B, show a high linear correlation with an R^2 values of 0.91 and RMSE of 8.35%. Each point in the graph represents an average flow cytometry measurement of six replicates and qOBM-feature averages of three replicates for each of the 36 different experimental conditions (four time-points, three PDTs cell lines, and three treatment groups). The linear regression model can also be used to compare the predicted qOBM cytotoxicity to the ground-truth flow cytometry viability data for each condition individually, rather than as an aggregate. Figures 4D–4F plot the individual results, which show remarkable agreement, with none of the pairs exhibiting statistically significant differences ($p > 0.05$) between the flow cytometry viability and the qOBM predicted cytotoxicity for any of the individual experimental conditions. Interestingly, while the different patient-derived cell lines contain distinct mutational profiles (detailed in [Supplement 1](#), Table S2), the regression model works equally well for all cell lines. A list of the p -values for all 36 experimental conditions can be seen in [Supplement 1](#), Table S3.

As a demonstration of the unique capabilities of the image-based cytotoxicity assay, we applied the model to predict the cytotoxicity of the CAR-T treated spheroid imaged continuously for 3 days inside of the incubator ([Visualization 13](#)). Again, for this spheroid, images were taken every 10 s for 3 days. From the continuous time-lapse images, features were extracted and fed into the linear regression model developed using the spheroids imaged daily (at four distinct time points). As seen in Fig. 4C, this process yields a continuous, non-destructive, non-endpoint measurement of spheroid cytotoxicity *in vitro*. While a one-to-one ground-truth comparison is impossible to obtain, we observe similar cytotoxicity measurements as seen in the endpoint flow cytometry data (which required >200 spheroids across four time points). Importantly, the continuous acquisition of image-based cytotoxicity data allows unprecedented longitudinal insight into spheroid health dynamics and effects of time and treatment. For example, in the first few hours of treatment, we see a rather turbulent trend: as seen in [Visualization 13](#), the spheroid appears to be settling within the well. As such, we attribute this inconsistency to the turbulent nature associated with the settling of the spheroid and CAR-T cells in the chamber. After settling, the qOBM-predicted cytotoxicity appears more constant. During this time (3–24 h), the CAR-T cells begin infiltrating into the spheroid, and we can see localized

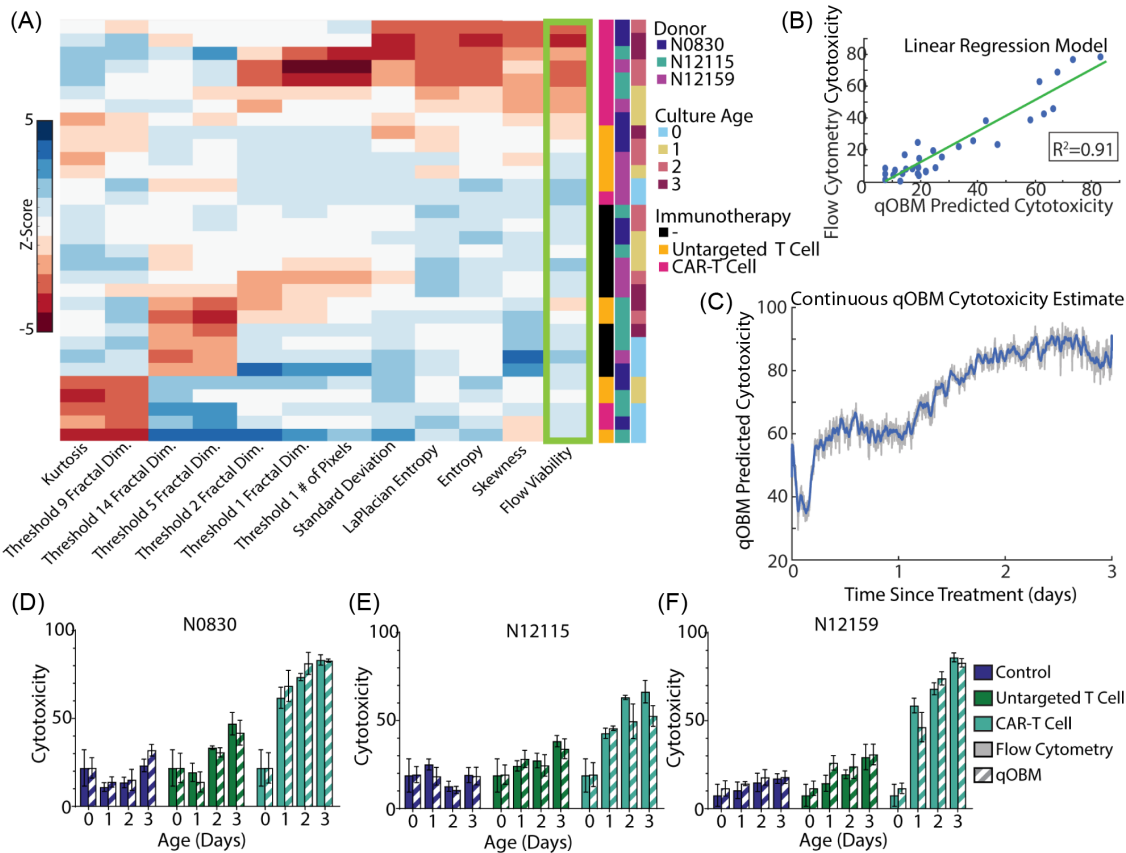


Fig. 4. Creation of a Linear regression model to predict cytotoxicity of immunotherapy-treated spheroids. (A) shows a clustergram comparing the static qOBM image features versus the flow cytometry cytotoxicity. Side labels demonstrate the culture treatment, donor, and age. Here, Thresholds 1, 2, and 5 contain refractive indices between 1.33 and 1.34, Threshold 9 contains refractive indices between 1.34 and 1.35, and Threshold 14 contains refractive indices between 1.35 and 1.36. (B) shows a linear regression model based on the data in the clustergram. (C) shows the continuous cytotoxicity estimate of a spheroid exposed to CAR-T cell treatment over 3 days. Gray lines show the standard deviation of cytotoxicity ± 10 min of imaging. (D)–(F) compare the flow cytometry cytotoxicity against the qOBM predicted cytotoxicity for each time point, each patient cell line, and each treatment condition.

cell death on the outer edges of the spheroid; however, the CAR-T cells do not appear to infiltrate deeper into the spheroid, leading to a fairly constant cytotoxicity value. After ~ 1 day, the qOBM predicted cytotoxicity increases asymptotically. During this time, we see the T cells infiltrating into the center of the spheroid imaged plane and attack the GBM cells. Around Day 2 the cytotoxicity appears to reach an asymptotic limit near 100%. At this point, the GBM cells on the imaging plane appear to be largely dead, while T cells continue to rummage through the spheroid. While we believe that cell killing continues deeper in the spheroid, the imaging plane here was focused on a region $\sim 50 \mu\text{m}$ deep in the spheroid. As such, the plateau seen here may account for localized cell death as opposed to spheroid-wide death, but, as shown in Figs. 4D–4F, it is nevertheless an excellent surrogate for flow cytometry-based viability assessments.

D. qOBM Applied to Visualize and Quantify Radiation and Chemotherapy Treatments in GBM Spheroids

Expanding on the visualization and quantitative analysis for T cell immunotherapy above, we now set out to establish the ability of qOBM to assess spheroid cell death in response to more standard treatments. Here, the treated groups included three different patient-derived spheroids with TMZ (1000 μm) chemotherapy, an experimental glycosaminoglycan drug—Surfen (20 $\mu\text{m} \pm$), and

radiation ($50 \text{ J/m}^2 \pm$). We imaged these spheroids once daily from Day 0 (immediately after treatment) to Days 1–3 post-treatment, with an additional control (no treatment) measurement. As shown in Figs. 5A–5H, a number of important structural differences can be observed between spheroids exposed to treatment versus the control. The control spheroid exhibits distinct, round cells, with well-defined large nuclei and prominent nucleoli (Fig. 5A). Spheroids treated with TMZ, on the other hand, show cells with a shriveled appearance (Figs. 5C, 5D and 5G, 5H), and those treated with Surfen develop holes within cells (Figs. 5B, 5D, 5F, and 5H). Interestingly, spheroids treated with radiation exhibit a buildup of high RI material which is consistent with our prior studies using qOBM for the analysis of human brain tumors treated with radiation (Figs. 5E–5H) [33]. We underscore that many of these unique features are not observed—or are not as appreciable—using traditional high-resolution imaging methods, including fluorescence, histology, and immunohistochemistry.

Next, we can compare our qOBM images with those taken with confocal fluorescence microscopy. As indicated by the pink arrows in Fig. 5I, confocal microscopy and qOBM clearly reveal cell nuclei; however, qOBM images exhibit superior access to sub-nuclear structures (like nucleoli) that are not visible without a separate dedicated label in confocal microscopy. Similarly, as indicated by the orange arrows in Figs. 5I and 5J, qOBM provides comparable visualization of polymerized actin relative to confocal

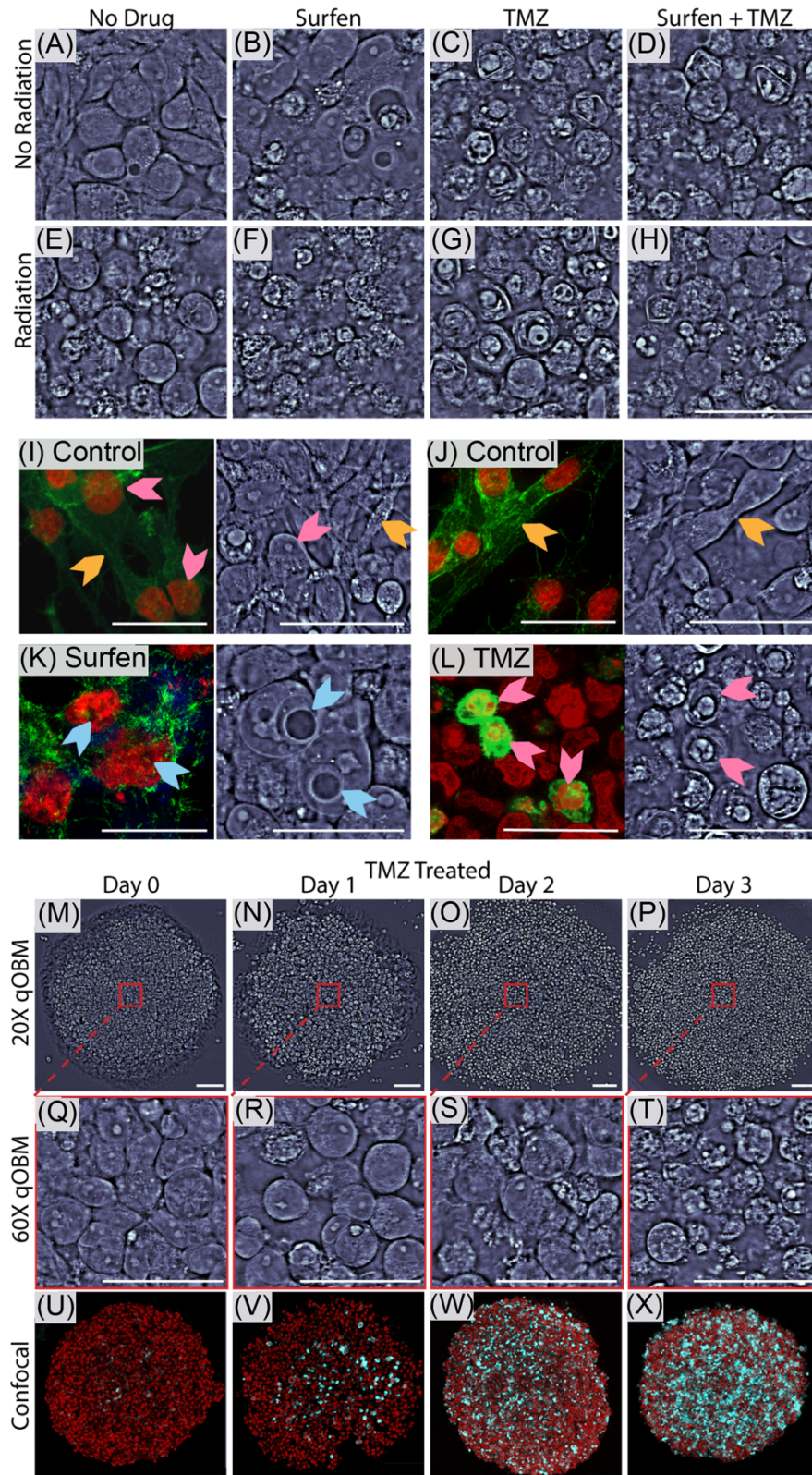


Fig. 5. Visualization of chemotherapy treated spheroids. (A)–(H) show the impact of all combinations of treatment after 3 days. Treatments include radiation (\pm), Surfen (\pm), and TMZ (\pm). (I)–(L) show comparisons of control (I), (J) and chemotherapy treated (K), (L) spheroids imaged with confocal microscopy and qOBM. Confocal images here are stained with propidium Iodide to label nuclei (red) and actin phalloidin to label cytoskeleton (green). In (I), (J), the pink arrows show nuclei, and the orange arrows show cytoskeleton. The blue arrows in (K) show the holes carved by Surfen. The pink arrows in (L) show chemotherapy-killed cells. (M)–(X) compare TMZ-treated spheroids over 3 days. (M)–(P) show low-magnification, 20 \times qOBM regions. (Q)–(T) show higher-magnification, 60 \times qOBM images of the same regions seen in (M)–(P). (U)–(X) show comparable confocal images. Here, confocal images are stained with DRAQ5 (red) to label nuclei and propidium Iodide (cyan) to label dead cells. Scale bars for (A)–(L) and (Q)–(T) are 50 μ m. Scale bars for (M)–(P) and (U)–(X) are 100 μ m. (A)–(H) are from cell line N12159, (I)–(X) are from cell line N0830.

fluorescence (baring color). In some cases, qOBM shows distinct puncta along these processes which are indicative of mass transport [34,35]. Such structures are unfortunately not visible with traditional confocal assays for spheroids. Moreover, the effects of the experimental Surfen treatment, which result in seemingly perforating holes through GBM cells nuclei (Fig. 5K), are far more apparent using qOBM than confocal fluorescence using traditional nuclear stains (see orange arrows). Additionally, we can identify shriveled, dead cells in 5L from TMZ-treatment. While molecular information is lacking with qOBM, it provides improved structural detail and can be readily applied continuously and longitudinally.

Figures 5M–5T show a TMZ-treated spheroid imaged over 3 days with a low-magnification 20 \times objective (M-P) and a high-magnification 60 \times objective (Q-T). The 20 \times magnification provides visualization of the macrostructure of the spheroid similar to that provided by a DRAQ5 nuclear stain (red) using confocal microscopy (5U–5X). As seen by the propidium iodide stain (cyan) in Figs. 5U–5X, cell death increases over the course of treatment, which can also be clearly visualized in the 60 \times qOBM images via cell fragmentation and cellular debris, again, expressed as high-RI content [36].

Next, we sought to employ functional imaging of each spheroid with dynamic qOBM (DqOBM) (imaging at 8 Hz for 75 s) [30,37]. For each spatial pixel in the dynamic image stack, we take the Fourier transform of the temporal-phase variations, as seen in Fig. 6B. Given the power-law nature of the frequency response of the phase values, we opt to plot each pixel's dynamic signal in phasor space (Fig. 6C). The phasors can be used to render color to indicate activity, as seen in Fig. 6C, with more dynamic regions represented in red and lower dynamic regions represented in dark blue. More details regarding DqOBM can be found in the methods and references [30,37]. To visualize the dynamic features along with the static phase values, we use an HSV map with the hue representing the dynamics, the saturation representing the static phase, and the value set to 1. Figures 6D–6K and 6P–6S show the results from various groups at Day 3 post treatment, where the control group (no treatment) clearly has the highest activity and the radiation + TMZ + Surfen-treated spheroids have the lowest activity. We note that DqOBM functional imaging was not used to analyze T cell therapy-treated spheroids because the strong directional motility of the T cells is not conducive to the pixel-wise temporal analysis of DqOBM.

Figures 6P–6S show the DqOBM images and phasor plots (L–O) of a single spheroid treated with radiation + Surfen + TMZ from day 0 to day 3 (DqOBM images of other groups over the 3 days post-treatment can be seen in [Supplement 1](#), Section 3 and [Supplement 1](#), Figure S2). These results clearly demonstrate that dynamic activity can be applied as an indicator of spheroid viability. As seen in Fig. 6T, a strong linear correlation exists between the flow cytometry viability and the center of mass of the phasor histogram. We can further quantify this analysis by computing the total signal energy captured in the frequency response of the dynamic signals, in this case using the area under the curve of the dynamic frequency response from 0.1 Hz (to remove the normalized DC component) to 4 Hz (half of our sampling frequency) (see Fig. 6U) [38]. This region is visualized as the shaded region in Fig. 6U. By directly comparing this signal energy to the flow cytometry viability, we see a high linear correlation with $R^2 = 0.71$ (Fig. 6V).

As with immunotherapy-treated spheroids, we leverage image features from the quantitative phase values and now add the

dynamic signals to estimate the viability of spheroids. As before, we first conducted a viability assessment of the spheroids using flow cytometry (used as ground truth). The results of the average viability for each of the three patient cell lines can be seen as solid bars in Figs. 7D–7F. Here, we see for all cell lines and treatments, viability decreased over the course of 3 days, with the lowest viability of spheroids observed with combined radiation + Surfen + TMZ treatment. These results not only confirm the effectiveness of the combined treatment but also set the stage, as shown below, for a deeper analysis of qOBM's potential to provide detailed, real-time insights into cell death progression.

Figure 7A shows the clustergram of select features which clearly shows a strong correlation the flow cytometry viability. We see the control spheroids and early time-point (Day 0 and Day 1) spheroids cluster together toward the top of the clustergram with higher viability. Meanwhile, the spheroids with greater amounts of cell death (lower viability) with more intense treatment regimens at later days cluster together toward the bottom of the clustergram. Using these variables, we created a linear regression model. Input variables comprised the average of three spheroids per condition using qOBM, and the response variable is the average flow viability of six different spheroids under identical conditions. This linear regression model was able to predict the average viability with a root mean square error (RMSE) of 7.2% and an R^2 of 0.89.

We then sought to observe the behavior of the model applied to individual spheroids. As seen in Fig. 7C, we can track the predicted viability for a single spheroid growing continuously. Again, this is not possible with flow cytometry measurements, as they are destructive end-point measurements. The regression results, while lacking ground truth from the same exact spheroids, are consistent with the trends seen among the flow cytometry data of six biological replicates (per condition and time point): the control spheroids remain with high viability followed by the spheroids treated with radiation and/or a single drug/chemotherapy agent, and the lowest viabilities belong to the spheroids treated with Surfen + TMZ or radiation + Surfen + TMZ.

Finally, Figs. 7D–7F plot the flow cytometry viability values (solid bar) and the qOBM predicted viability values (striped bar) for all the experimental permutations, individually. Again, the qOBM predicted values are the average of three spheroids, and the flow cytometry values are the average of six different spheroids. Remarkably, none of the qOBM estimates and corresponding flow cytometry-pair measurements exhibit statistically significant variations—a full analysis of all P -values can be seen in [Supplement 1](#), Table S4. The lack of significant differences between qOBM and flow cytometry viability measurements demonstrates the significant potential of this model to be applied to different cell lines and treatments.

3. DISCUSSION AND CONCLUSION

qOBM achieves continuous and longitudinal, non-invasive, label-free quantitative imaging of live patient-derived tumor spheroids with functional information and unprecedented sub-cellular detail. The unique quantitative information provided by qOBM enables longitudinal assessment of the effects of GBM treatments—including, chemoradiotherapy using UV radiation and TMZ, an experimental bis-4-aminoquinoline drug—Surfen, and cellular immunotherapy—with remarkable agreement with end-point flow cytometry measurements of viability and cytotoxicity. The simple instrumentation of qOBM also enables the use of

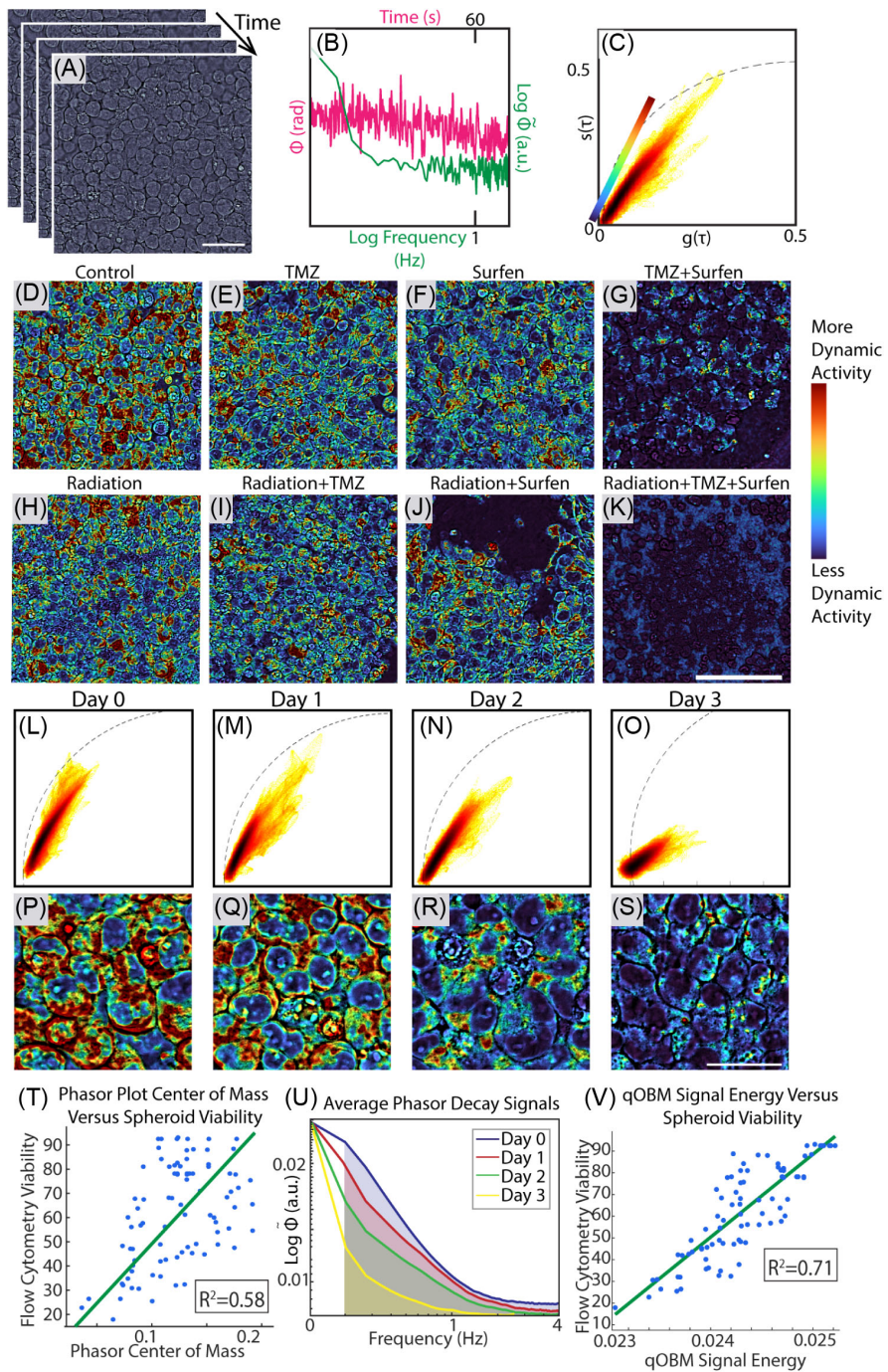


Fig. 6. Phasor plots reveal distinct frequency-domain signatures of spheroid dynamics, with a shift toward lower dynamic activity in treated spheroids, indicative of reduced cellular motility and apoptosis. (A)–(C) show how DqOBM is calculated. (D)–(K) show and colorized DqOBM images of a spheroid monitored over the course of 3 days. (L)–(S) show corresponding phasor plots and colorized DqOBM images from a single spheroid over time. (T) shows the center of mass of the spheroid plotted against the flow cytometry. (U) shows the phasor decay signal of the spheroid. Shaded area shows the region summed to comprise signal energy of the dynamic decay. (V) shows the qOBM signal energy versus the flow cytometry viability. Scale bar in (D)–(K) is 100 μm . Scale bar in (P)–(S) is 50 μm . (D)–(K) are from cell line N12159, (P)–(S) are from a single spheroid from cell line N12115.

a low-cost, compact system that can be placed within a standard incubator to facilitate use and adoption. Together, qOBM offers unprecedented capabilities for monitoring spheroids which can open new avenues of inquiry for fast, high-throughput evaluation of treatments for GBM and other malignancies.

In the analysis presented here, we utilized three different patient-derived GBM cell types, each with distinct mutational profiles and stemness markers, as outlined in [Supplement 1](#), Table S2.

These glioma stem cells (GSCs) exhibit clinically relevant mutations, such as EGFR amplification and PTEN deletion, and express varying levels of GD2, CD133, and CD44 antigens. Despite these genetic and phenotypic differences, the qOBM-derived linear regression model used to predict viability of radiation and chemotherapy-treated spheroids combined data from all cell types and treatments, suggesting that the model can be applied widely to other spheroids and treatments. Indeed, we observed unique

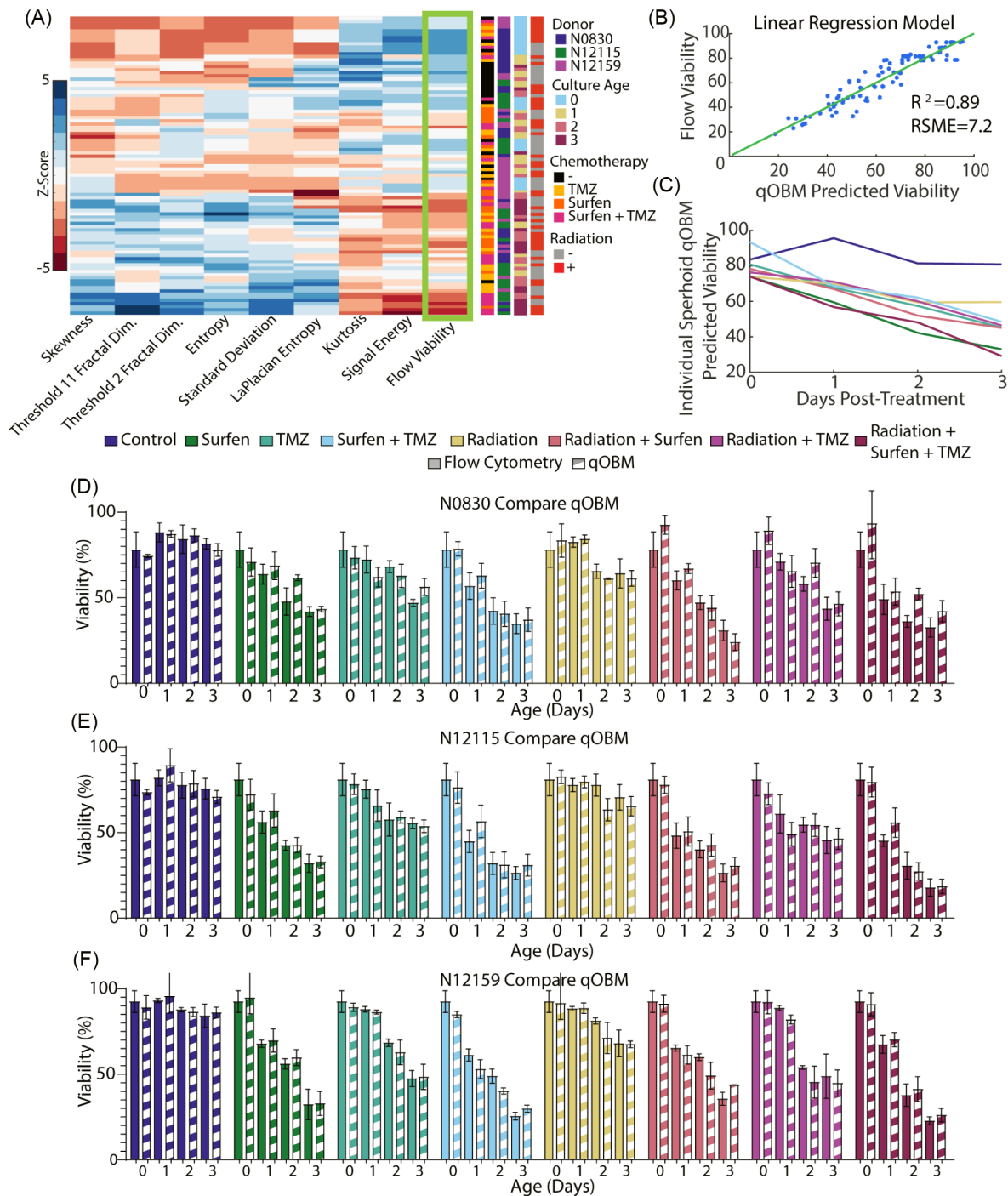


Fig. 7. Creation of a linear regression model to predict the viability response of drug- and radiation-treated spheroids. (A) shows a clustergram comparing the static and dynamic qOBM image features versus the flow cytometry viability. Here, Threshold 2 contains refractive indices between 1.33 and 1.34, and Threshold 11 contains refractive indices between 1.34 and 1.35. (B) shows a linear regression model based on the data in the clustergram. (C) tracks the viability of a single N12159 spheroid over time (1 of each treatment). (D)–(F) compares the flow cytometry viability against the qOBM predicted viability for each time point, each patient cell line, and each treatment condition.

effects from different treatment types (e.g., the “holes” in the cells with Surfen or the shriveled dead cells with TMZ, see Fig. 5), but the model seems to mostly use the texture and morphology of dead cells to determine the health of the spheroid. Dead cells and cellular debris with qOBM appear with higher refractive index values and a lack of clear circular cells and nuclei. Such structures are readily captured with texture and fractal features, as well as the overall phase image entropy, a measure of the information content.

This model also included DqOBM functional information that is not applicable to T cell therapy as the strong directional motility of the T cells is not conducive to the pixel-wise temporal analysis of DqOBM. (In *Supplement 1*, Section S5, we show a separate dynamic analysis using dispersion-relation phase spectroscopy (DPS) [34]; however, this analysis did not provide predictive power.) Nevertheless, the T cell-specific model—one for all three cell lines—used similar texture parameters from qOBM images to

predict cytotoxicity, again suggesting the approach can be applied to highly diverse PDTs under this type of treatment.

A significant implication of our predictive models is that qOBM can now provide an in-line estimate of cytotoxicity/viability of a spheroid continuously (every few seconds) and longitudinally (over days). This allows us to gain unique insight into the spheroid health and treatment efficacy with unprecedented temporal resolution. In fact, the results presented in [Visualization 13](#), and accompanying quantitative cytotoxicity estimates ([Fig. 4C](#)), show extremely complex behavior of T cells attacking GBM spheroids over 3 days, with quantitative cytotoxicity estimates indicating an initial plateau region and then an asymptotic region. To our knowledge, this is the first time such behavior has been recorded (videos of T cells in spheroids and cytotoxicity response). We also observed that CAR-T cells traverse the spheroids at faster speeds and with more complex paths than untargeted T cells. Our quantitative imaging and analysis capabilities open the door to new types of experiments that can analyze, in real-time, the response to changes in experimental conditions, such as treatments, environment, nutrition, stimuli, temperature, etc., which was previously not possible. In future work, we expect to achieve real-time 3-D volumetric imaging which could also enable additional insight, such as 3D-tracking of T cells.

In this work, one of the major treatments studied with qOBM was CAR-T cell therapy, which remains an emerging treatment modality. While CAR-T cell therapy has shown promise in other malignancies, its efficacy in GBM has been limited due to issues related to intratumoral antigen heterogeneity, an immunosuppressive tumor microenvironment, and poor CAR-T cell persistence [[19](#)]. Spheroid models serve as a valuable platform for studying T cell infiltration, proliferation, and cytotoxicity within a physiologically relevant 3D tumor microenvironment [[39,40](#)]; however, several critical gaps remain in understanding the effectiveness of CAR-T cell therapy, including the extent of T cell infiltration and migration through dense GBM tissues, the kinetics and complexity of their movement within the tumor microenvironment, and the influence of patient-derived tumor characteristics on therapeutic efficacy [[41](#)]. As shown in this work, the dynamics of the T cells with the cancer cells are highly complex and not yet well understood given that such behavior had never been captured in 3D cell cultures. As demonstrated in this work, qOBM is uniquely positioned to address these critical questions and enable a better understanding of these interactions in the future.

Indeed, other optical methods have been employed for imaging 3D spheroids and organoids including confocal imaging, other forms of quantitative phase imaging (QPI), dynamic full field (DFF)-OCT, and FLIM; however, these methods have important limitations. Confocal imaging requires labeling the spheroids with fluorescence agents and suffers from phototoxicities and photo-bleaching, making longitudinal monitoring challenging. Other QPI techniques that deliver similar subcellular detail operate in transmission mode and thus are limited to thin samples (less than $\sim 100 \mu\text{m}$), even when advanced computational methods are applied to compensate for scattering [[42](#)]. DFF-OCT can provide similar levels of cellular and dynamic detail as qOBM with a similar penetration depth ($\sim 200 \mu\text{m}$); however, DFF-OCT is extremely data intensive and relies on expensive and complex components [[43](#)]. Compared to DFF-OCT, qOBM has improved subcellular contrast, the imaging rate is $10^2\text{--}10^4$ times faster, and the data requirements are $10^2\text{--}10^3$ less stringent. DFF-OCT may also not

be applicable to imaging immunotherapy treatments, as the T cells' fast movement may prohibit analysis with this technique. While any dataset capturing cell movement continuously for 3 days with a sampling frequency of 10 s is large in nature, the qOBM images are based on four captures and do not require large amounts of processing power to produce. Although DFF-OCT has also been built around a sophisticated microscope system with a stage-top incubator [[44](#)], the low-cost compact qOBM system presented here, which fits inside standard incubators, provides significant advantages for user adoption and experimental versatility. Finally, FLIM has been previously used as a label-free method to evaluate the treatment response of spheroids and organoids; [[45](#)] however, FLIM is bulky, expensive, slow, has limited throughput, and suffers from phototoxicity. While qOBM imaging does not contain the biomolecular specificity obtained with FLIM, qOBM does enable long-term, continuous, and fast dynamic imaging. While these methods have been extremely valuable, qOBM overcomes significant limitations of previous methods and provides unique capabilities.

In conclusion, this work presents qOBM as a novel tool to observe and quantitatively analyze patient-derived tumor spheroids and evaluate treatments. The subcellular contrast provided by qOBM is unprecedented for a label-free, non-invasive, and low-cost modality, which enables unique continuous and longitudinal imaging capabilities under physiological conditions (inside an incubator). To our knowledge this is the first time that the effects of immunotherapy, chemotherapy, or radiation have been observed with subcellular detail, non-invasively, and without labels, and quantified to enable predictive models of viability/cytotoxicity. We expect qOBM to become an important new tool to analyze PDTs and evaluate personalized treatments.

4. METHODS

A. Spheroid Culture

Patient-derived GBM cell types (N0830, N12115, and N12159) were maintained in complete GSC medium including Neurobasal A Medium (Thermo Fisher Scientific, Waltham, Massachusetts, USA) supplemented with 1% penicillin-streptomycin (Corning, New York, New York, USA), 0.5% GlutaMax, 1% N2 (Gibco, Montana, MT, USA), 2% B-27 (Gibco, Montana, MT, USA), 10 ng/mL bFGF (R&D Systems, Minneapolis, Minnesota, USA), 20 ng/mL hEGF (Abcam, Waltham, Massachusetts, USA), and 0.4% heparin (StemCell Technologies, Vancouver, British Columbia, Canada) and then seeded for spheroid formation with a 20,000 cells/well density in 96-well round-bottom ultra-low attachment plates (Corning, New York, New York, USA). The culture plates were incubated under standard cell culture conditions (37°C , 5% CO_2 , and 95% relative humidity) for 48 h to allow spheroid formation prior to initiating drug treatment or co-culture with T cells.

B. Spheroid Treatment Conditions

After 48 h of spheroid formation, the spheroids were transferred to customized polydimethylsiloxane (PDMS) culture devices for treatment. The device is a custom PDMS culture insert bonded to a glass slide and configured as an open-well chamber array. Six small-volume cylindrical chambers (4 mm diameter, 7 mm height, 90 μL) confine individual GBM spheroids within the

working distance and field of view of the qOBM objective while allowing rapid media exchange and delivery of therapeutic agents by pipetting. Thus, the device functions as a microscale, optically optimized culture platform that standardizes spheroid positioning and imaging conditions for qOBM. Spheroids were exposed to varying concentrations of temozolomide (TMZ; 500, 1000, and 2000 μM), bis-2-methyl-4-amino-quinolyl-6-carbamide (Surfen; 10, 20, and 40 μM), and radiation (Stratalinker, UV 254nm; 5, 10, and 20 mJ/cm^2). Treatments were conducted in the same complete medium used for spheroid culture, ensuring consistency across experimental conditions. The spheroids were maintained in these conditions for 72 h, with qOBM imaging conducted every 24 h and flow cytometry or confocal microscopy after 72 h.

C. T Cell Culture

T cells were isolated from healthy donors as approved by the institutional review board of the University of Wisconsin-Madison (2018-0103) as previously described [46]. Later, anti-GD2 CAR-T and untargeted T cells were prepared using a virus-free method [47], cryopreserved at 5M cells/vial in 90% FBS and 10% DMSO, and shipped on dry ice to the University of Georgia for this research. After thawing the anti-GD2 CAR-T and untargeted T cells briefly in a 37°C water bath, they were rapidly transferred to 9 mL of pre-warmed ImmunoCult-XF T cell Expansion Medium (StemCell Technologies, Vancouver, British Columbia, Canada), centrifuged at 200 $\times g$ for 3 min, resuspended in ImmunoCult-XF Medium, and counted with Trypan Blue to assess viability. Cells were then cultured for 24 h at a density of 1 million cells/mL in ImmunoCult-XF Medium, supplemented with 200 IU/mL Human IL-2 Recombinant Protein (PeproTech) and stimulated with 25 $\mu\text{L}/\text{mL}$ of Human CD3/CD28 Activation Serum (StemCell Technologies). The next day, the activation serum was removed, and the cell density was adjusted to 1 million cells/mL. Both CAR T and control T cells were maintained in the ImmunoCult-XF Medium supplemented with 200 IU/ml Human Recombinant IL-2 for about 7 days until they reached optimal viability for experiments. T cells were counted and adjusted on the same day as the spheroid seeding to maintain a 1:1 effector-to-target (E:T) ratio at the time of co-culture.

D. Immunocytochemistry and Confocal Imaging

At designated time points (Days 0–3), PTDSs were fixed and permeabilized using either BD Cytofix/Cytoperm (BD Biosciences) or Fixation/Permeabilization buffer (BioLegend), applied for 15 min at room temperature according to the respective manufacturer's instructions. After fixation, spheroids were washed three times with phosphate-buffered saline (PBS) and then incubated in blocking buffer composed of 5% bovine serum albumin (BSA) in PBS with 0.1% Tween-20 (PBST) for 30 min at room temperature to minimize nonspecific binding.

For immunostaining of CAR-T and GBM co-cultures, spheroids were incubated in a primary staining solution prepared in blocking buffer containing PE/Cy7-conjugated anti-Granzyme B (1:100 dilution), APC-conjugated anti-GD2 (1:100 dilution), and Alexa Fluor 488-conjugated Actin-Phalloidin (1:100 dilution). The staining was carried out either for 1 h at room temperature or overnight at 4°C, protected from light. Nuclear labeling was performed using DAPI (1 $\mu\text{g}/\text{mL}$ in PBS; 1:1000

dilution) for 10 min, followed by a final wash in PBS before imaging.

For chemotherapy- and radiation-treated spheroids, nuclear integrity, cytoskeletal organization, and cell viability were assessed using a different panel of dyes. Samples were incubated with propidium iodide (PI, 1:1000 dilution) to stain dead cells, DRAQ5 (1:600 dilution) as a far-red nuclear stain, and Alexa Fluor 488-conjugated Actin-Phalloidin (1:100 dilution) to visualize the actin cytoskeleton. All dyes were prepared in PBS and incubated for 30 min at room temperature, protected from light. Following staining, spheroids were washed once with PBS and mounted using Fluoromount-G (SouthernBiotech).

All samples were imaged using a Zeiss LSM980 confocal microscope with Airyscan2. Fluorophores were excited using laser lines at 405 nm (Hoechst 33342 and DAPI), 488 nm (AF488), 561 nm (PE/Cy7, PI), and 639 nm (APC, DRAQ5). Z-stack images were acquired using 20 \times and 60 \times objectives under consistent acquisition settings for all groups. Image processing and analysis were performed using FIJI/ImageJ for maximum intensity projection, channel separation, brightness/contrast adjustment, and qualitative structural evaluation.

E. Flow Cytometry

Flow cytometry was employed to assess cell viability and apoptosis post-treatment. For drug treatment assays, GSC cell viability was assessed using eFluor450 fixable viability dye (Thermo Fisher Scientific, Waltham, Massachusetts, USA). In co-culture experiments with T cells, apoptosis was analyzed using the Annexin V-FITC/PI apoptosis kit (Abnova, Taipei, Taiwan). The CAR transgene of T cells was identified using the 1A7 anti-14G2a idiotype antibody (National Cancer Institute Biological Resources Branch) conjugated to APC with the Lightning-Link APC antibody labeling kit (Novus Biologicals), with staining performed according to the manufacturer's instructions. Dead cells were stained with PI, while apoptotic cells were stained with Annexin V-FITC. All antibody staining was conducted in FACS Buffer (1 \times PBS containing 2% FBS), and the data were acquired on a NovoCyte Quanteon flow cytometer (Agilent Technologies, Santa Clara, California, USA) and processed with FlowJo 10.7.1 software (Becton Dickinson, Franklin Lakes, New Jersey, USA).

F. Quantitative Oblique Back-Illumination Microscopy

The qOBM system consists of a conventional brightfield microscope with a modified illumination module [27–29,48]. Rather than the classic transmission-based illumination used in brightfield microscopy and QPI, qOBM illuminates samples in epi-mode using four LED light sources (720 nm) deployed through multi-mode optical fibers arranged around the objective, 90° from each other. Through these fibers, the sample is illuminated in epi-mode, where approximately 45 mW are incident on the organoid samples. In the organoids, the photons undergo multiple scattering events causing the photons to change direction, with some being redirected back toward the microscope objective. These redirected photons create an effective virtual light source within the sample with an overall oblique illumination, a process known as oblique back-illumination [49]. Variations in the index of refraction in the sample refract the light either toward or away from the microscopy objective, resulting in intensity fluctuations that encode the RI properties of the sample. This work uses a Nikon S Plan Fluor

LWD 99 20 \times , 0.45 NA and Nikon S Plan Fluor LWD 40 \times , 0.6 NA. Light collected by the microscope is detected using an sCMOS camera (pco.edge 4.2 LT). Intensity images collected from two opposing illumination angles are subtracted to produce a differential phase contrast (DPC) image. Two orthogonal DPC images (a total of four acquisitions) are deconvolved with the system's optical transfer function to finally obtain quantitative phase contrast images. This process has been described in further detail in previous studies [27–29,48,50].

G. Compact qOBM System

The compact, incubator-compatible qOBM system operates on the same principles as the system described above. Several substitutions are made to make this system low-cost and suitable for the incubator. First, the pco.edge camera is substituted with a Basler Ace acA3088-57um USB 3.0 Monochrome Camera. The stage here is controlled with a simple XYZ stage (ThorLabs LX30) and stepper motors/motor drivers mounted within the incubator. The LEDs and all electronic controls are mounted outside the incubator. The multimode fibers deliver the LED light to the sample and all electronics are triggered via cables fed through the incubator port. An external PC is used to control all components both within and outside of the incubator.

H. Dynamic Quantitative Oblique Back-Illumination Microscopy

To conduct functional imaging with qOBM, we have developed Dynamic qOBM (DqOBM) [30]. In DqOBM a sample is imaged over a period of time—for all samples in this work this time period is 75 s at 8 Hz to obtain 600 images. From these images, we obtain a pixel-wise dynamic frequency response given by the absolute value of the Fourier transform of the temporal phase signal, $\tilde{\phi}(f) = |\mathcal{F}\{\phi(t)\}|$ for each spatial pixel in the image. We observe that the frequency response of the pixels exhibits an exponential or multi-exponential decay indicative of subcellular mass movement that more prominently oscillates at low frequencies and dampens exponentially with increasing frequency. This functional behavior is expected for cell structures such as cell membranes [51] and mitochondria [52], among other structures [53]. As expected, the dynamic response in background regions shows a mostly flat near-zero amplitude dynamic response, indicative of static behavior.

To visualize the cell dynamics, we utilize phasor analysis [54,55], as it aligns well with the exponential nature of the dynamic phase frequency response, $\tilde{\phi}(f)$. Phasor analysis is a widely used technique for examining spectral and dynamic signals, especially those with exponential characteristics, such as those encountered in fluorescent lifetime and pump-probe microscopy [54,55]. This method involves decomposing signals into two variables, typically referred to as g and s , which are derived from the cosine and sine transforms (real and imaginary components of the Fourier Transform) of the dynamic signals (here $\tilde{\phi}(f)$) for each spatial pixel in the image at a particular period, τ . In our case, we choose $\tau = 0.5$ s depending on the net acquisition rate to decompose the signals into g and s following Eqs. (1) and (2), respectively,

$$g_i(\tau) = \frac{\int \tilde{\phi}_i(f) \cos(2\pi f\tau) df}{\int \tilde{\phi}_i(f) df}, \quad (1)$$

$$s_i(\tau) = \frac{\int \tilde{\phi}_i(f) \sin(2\pi f\tau) df}{\int \tilde{\phi}_i(f) df}. \quad (2)$$

In phasor space, the two components, g and s , act as coordinates, uniquely defining each pixel in the image. As a result, the phasor plot represents a 2D histogram that captures the distribution of g and s values across the image. Similar dynamic signals tend to cluster together in this space, while mixtures of exponential signals create linear mappings between regions. The boundary points of these distributions are termed endmembers.

The cumulative phasor plot in Figs. 6L–6O shows signals that lie mostly within the universal semicircle (black dotted line in Figs. 6L–6O), which signifies that the frequency response of the cellular dynamics, for the most part, follows an exponential behavior [54,55]. But because the frequency response is not physically constrained to be strictly exponential, some signals are observed outside the universal semi-circle (but they are within the unit circle due to the normalization of g and s). Figures 6L–6O also show the average responses from two distinct regions in phasor space.

The dynamic signal energy was calculated in accordance with Eq. (3). This signal energy is represented at the area under the curve of a phasor line decay:

$$E_{\text{signal}} = \sum_{0.1 \text{ Hz}}^{4 \text{ Hz}} |\tilde{\phi}(f)|^2. \quad (3)$$

In this paper, we integrate the signal from 0.1 to 4 Hz, as seen in Fig. 6U.

I. Image Feature Extraction

Quantitative image features extracted from the qOBM images were analyzed to assess the structural differences occurring in the treated spheroids. To accomplish this, features images from the 60 \times , 0.7 NA objective (280 $\mu\text{m} \times 280 \mu\text{m}$) were extracted from all in-focus images based on texture analysis [56], fractal analysis [57], Fourier space features [58], and mathematical auto-correlation transformations [59,60]. Detailed explanations regarding the computed features can be found in Ref. [48]. In terms of selecting thresholds for fractal analyses, phase shift values were split into eight equally spaced divisions ranging from phase shifts of -0.3 to 2. Utilizing the phase to refractive index formula [61], this corresponds to refractive indices of ~ 1.33 –1.41. Feature values were correlated against the average flow cytometry values obtained from spheroids. Feature selection ranking was performed using the R^2 to determine the most significant features correlating with the flow cytometry values. The highest ranked features that correlated with an $R^2 > 0.55$ for the immunotherapy-treated spheroids and > 0.40 for the chemotherapy and radiation treated spheroids are discussed in the Results. A full analysis into the correlated features can be seen in Supplement 1, Figures S5 and S6.

J. Linear Regression Model Creation

Linear regression models were created in MATLAB using the image features described above and displayed in the clustergrams in Figs. 4 and 7 as the predictor data with a response variable of the flow cytometry data. The fitlm function was used to fit a linear model, with the flow cytometry data as the response variable and the corresponding predictor variables as the explanatory variables. This function calculates the best-fit line by minimizing the residual

sum of squares, producing a linear equation that represents the relationship between the predictors and the response. The model was assessed for statistical significance using the p-values and R-squared values, and residuals were checked to ensure the assumptions of linearity and homoscedasticity were met. Finally, the model was validated through visualization by plotting the fitted regression line, the qOBM feature-predicted viability, and the flow cytometry viability.

K. Statistical Analysis

In quantifying the differences between the qOBM estimates of cytotoxicity and viability, the average between six spheroids analyzed via flow cytometry was compared to the average of three spheroids imaged with qOBM. Unpaired T-tests were used to determine statistical significance ($p < 0.05$). A full list of the obtained P -values for each treatment comparison can be seen in [Supplement 1](#), Tables S3 and S4.

Funding. National Science Foundation Graduate Research Fellowship Program (NSF GRFP DGE-203965); Burroughs Wellcome Fund (CASI BWF 1014540); National Institute of General Medical Sciences (R35GM147437); National Science Foundation (EEC-1648035).

Acknowledgment. We acknowledge the Biomedical Microscopy Core and the Flow Cytometry Core at the University of Georgia for their support. We also extend our gratitude to Dr. Daniel J. Brat, Chair of the Department of Pathology at Northwestern University Feinberg School of Medicine, for generously providing the patient-derived GBM cells used in this study. Figure 1 was created in part with [62]. All experimental protocols utilizing human cells were conducted under the guidelines of the Georgia Institute of Technology. Anti-GD2 CAR-T cells were obtained for this study with logistical support from Ross Schwartz under the supervision of Dr. Krishanu Saha. C.E.S., A.D., L.K., and F.E.R. designed the experiments outlined in the paper. C.E.S. acquired the qOBM data, analyzed the data, developed the regression models used, and made all figures in the manuscript. A.D. designed flow cytometry and fluorescent imaging panels and acquired the confocal microscopy and flow cytometry data. A.D. and L.M. designed and fabricated the culture inserts. A.D. and D.M. performed cell cultures, co-cultures and analyzed flow cytometry results. Z.L. developed the application for the incubator system. D.C. and K.S. provided the CART and control T cells. C.E.S., A.D., L.K., and F.E.R. wrote and revised the paper. All authors reviewed the results and approved the final version of the paper.

Disclosures. K.S. is a member of the scientific advisory boards of Bharat Biotech and Andson Biotech.

Data availability. Data and code underlying the results presented in this paper are not publicly available at this time but may be obtained from the corresponding author upon reasonable request. Similarly, materials used in the study are largely outlined in the Methods section; however, further details may be obtained from the corresponding author upon reasonable request.

Supplemental document. See [Supplement 1](#) for supporting content.

REFERENCES

1. P. Y. Wen, M. Weller, E. Q. Lee, et al., "Glioblastoma in adults: a Society for Neuro-Oncology (SNO) and European Society of Neuro-Oncology (EANO) consensus review on current management and future directions," *Neuro-Oncology* **22**, 1073–1113 (2020).
2. Y. Li, P. Tang, S. Cai, et al., "Organoid based personalized medicine: from bench to bedside," *Cell Regen.* **9**, 21 (2020).
3. F. Jacob, R. D. Salinas, D. Y. Zhang, et al., "A patient-derived glioblastoma organoid model and biobank recapitulates inter- and intra-tumoral heterogeneity," *Cell* **180**, 188–204.e22 (2020).
4. G. Berkers, P. van Mourik, A. M. Vonk, et al., "Rectal organoids enable personalized treatment of cystic fibrosis," *Cell Rep.* **26**, 1701–1708.e3 (2019).
5. G. Vlachogiannis, S. Hedayat, A. Vatsiou, et al., "Patient-derived organoids model treatment response of metastatic gastrointestinal cancers," *Science* **359**, 920–926 (2018).
6. S. N. Ooft, F. Weeber, K. K. Dijkstra, et al., "Patient-derived organoids can predict response to chemotherapy in metastatic colorectal cancer patients," *Sci. Transl. Med.* **11**, eaay2574 (2019).
7. Y. Yao, X. Xu, L. Yang, et al., "Patient-derived organoids predict chemoradiation responses of locally advanced rectal cancer," *Cell Stem Cell* **26**, 17–26.e6 (2020).
8. K. Ganesh, C. Wu, K. P. O'Rourke, et al., "A rectal cancer organoid platform to study individual responses to chemoradiation," *Nat. Med.* **25**, 1607–1614 (2019).
9. H. Tiriac, P. Belleau, D. D. Engle, et al., "Organoid profiling identifies common responders to chemotherapy in pancreatic cancer," *Cancer Discov.* **8**, 1112–1129 (2018).
10. E. Driehuis, A. van Hoeck, K. Moore, et al., "Pancreatic cancer organoids recapitulate disease and allow personalized drug screening," *Proc. Natl. Acad. Sci. USA* **116**, 26580–26590 (2019).
11. L. Broutier, G. Mastrogiovanni, M. M. Verstegen, et al., "Human primary liver cancer-derived organoid cultures for disease modeling and drug screening," *Nat. Med.* **23**, 1424–1435 (2017).
12. Y. Saito, T. Muramatsu, Y. Kanai, et al., "Establishment of patient-derived organoids and drug screening for biliary tract carcinoma," *Cell Rep.* **27**, 1265–1276.e4 (2019).
13. S. H. Lee, W. Hu, J. T. Matulay, et al., "Tumor evolution and drug response in patient-derived organoid models of bladder cancer," *Cell* **173**, 515–528.e17 (2018).
14. S. J. Hill, B. Decker, E. A. Roberts, et al., "Prediction of DNA repair inhibitor response in short-term patient-derived ovarian cancer organoids," *Cancer Discov.* **8**, 1404–1421 (2018).
15. M. Akay, J. Hite, N. G. Avci, et al., "Drug screening of human GBM spheroids in brain cancer chip," *Sci. Rep.* **8**, 15423 (2018).
16. J. Balça-Silva, D. Matias, A. Do, et al., "Glioblastoma entities express subtle differences in molecular composition and response to treatment," *Oncol. Rep.* **38**, 1341–1352 (2017).
17. A. Segerman, M. Niklasson, C. Haglund, et al., "Clonal variation in drug and radiation response among glioma-initiating cells is linked to proneural-mesenchymal transition," *Cell Rep.* **17**, 2994–3009 (2016).
18. S. J. Bagley, A. S. Desai, G. P. Linette, et al., "Car Ts-cell therapy for glioblastoma: recent clinical advances and future challenges," *Curr. Protoc. Immunol.* **20**, 1429–1438 (2018).
19. P. Zhang, Y. Zhang, and N. Ji, "Challenges in the treatment of glioblastoma by chimeric antigen receptor T-cell immunotherapy and possible solutions," *Front. Immunol.* **13**, 927132 (2022).
20. S. Kessel, S. Cribbes, O. Déry, et al., "High-throughput 3D tumor spheroid screening method for cancer drug discovery using celigo image cytometry," *SLAS Technol.* **22**, 454–465 (2016).
21. M. Vinci, S. Gowar, F. Boxall, et al., "Advances in establishment and analysis of three-dimensional tumor spheroid-based functional assays for target validation and drug evaluation," *BMC Biol.* **10**, 29 (2012).
22. I. Rakotoson, B. Delhomme, P. Djian, et al., "Fast, multicolor 3-D imaging of brain organoids with a new single-objective two-photon virtual light-sheet microscope," *Front. Neuroanat.* **13**, 77 (2018).
23. F. Pampaloni, N. Ansari, and E. H. K. Stelzer, "High-resolution deep imaging of live cellular spheroids with light-sheet-based fluorescence microscopy," *Cell Tissue Res.* **352**, 161–177 (2013).
24. M. A. Lancaster and J. A. Knoblich, "Cerebral organoids model human brain development and microcephaly," *Nature* **350**, 373–379 (2013).
25. T. Kadoshima, H. Sakaguchi, T. Nakano, et al., "Self-organization of axial polarity, inside-out layer pattern, and species-specific progenitor dynamics in human ES cell-derived neocortex," *Proc. Natl. Am. Soc. USA* **110**, 20284–20289 (2013).
26. X. Qian, H. N. Nguyen, M. M. Song, et al., "Brain-region-specific organoids using mini-bioreactors for modeling ZIKV exposure," *Cell* **165**, 1238–1254 (2016).
27. P. Ledwig, M. Sghayyer, J. Kurtzberg, et al., "Dual-wavelength oblique back-illumination microscopy for the non-invasive imaging and quantification of blood in collection and storage bags," *Biomed. Opt. Express* **9**, 2743–2754 (2018).
28. P. Ledwig and F. E. Robles, "Epi-mode tomographic quantitative phase imaging in thick scattering samples," *Biomed. Opt. Express* **10**, 3605–3621 (2019).
29. P. Ledwig and F. Robles, "Quantitative 3D refractive index tomography of opaque samples in epi-mode," *Optica* **8**, 6–14 (2021).

30. P. C. Costa, B. Wang, C. Serafini, et al., "Functional imaging with dynamic quantitative oblique back-illumination microscopy," *J. Biomed. Opt.* **27**, 066502 (2022).
31. L. Lin, J. Couturier, X. Yu, et al., "Granzyme B secretion by human memory CD4 T cells is less strictly regulated compared to memory CD8 T cells," *BMC Immunol.* **15**, 36 (2014).
32. R. Y. Karimui, "A new approach to measure the fractal dimension of a trajectory in the high-dimensional phase space," *Chaos Solitons Fractals* **151**, 111239 (2021).
33. T. M. Abraham, P. C. Costa, C. Serafini, et al., "Label- and slide-free tissue histology using 3D epi-mode quantitative phase imaging and virtual hematoxylin and eosin staining," *Optica* **10**, 1605–1618 (2023).
34. R. Wang, Z. Wang, L. Millet, et al., "Dispersion-relation phase spectroscopy of intracellular transport," *Opt. Express* **19**, 20571–20579 (2011).
35. S. Pradeep and T. A. Zangle, "Quantitative phase velocimetry measures bulk intracellular transport of cell mass during the cell cycle," *Sci. Rep.* **12**, 6074 (2022).
36. C. E. Serafini, V. Gorti, P. Casteliero, et al., "Label-free in-line characterization of immune cell culture using quantitative phase imaging," *npj Regener. Med.* **10**, 56 (2025).
37. C. Serafini, M. Green, A. Diering, et al., "Label-free functional analysis of root-associated microbes with dynamic quantitative oblique back-illumination microscopy," *Sci. Rep.* **14**, 5812 (2024).
38. J. G. Proakis and D. G. Manolakis, *Digital Signal Processing. Principles, Algorithms, and Applications* (Prentice Hall, 1996).
39. T. Rodrigues, B. Kundu, J. Silva-Correia, et al., "Emerging tumor spheroids technologies for 3D in vitro cancer modeling," *Pharmacol. Ther.* **184**, 201–211 (2018).
40. S. Herter, L. Morra, R. Schlenker, et al., "A novel three-dimensional heterotypic spheroid model for the assessment of the activity of cancer immunotherapy agents," *Cancer Immunol. Immunother.* **66**, 129–140 (2017).
41. E. Skaga, E. Kulesskiy, A. Fayzullin, et al., "Intertumoral heterogeneity in patient-specific drug sensitivities in treatment-naïve glioblastoma," *BMC Cancer* **19**, 628 (2019).
42. O. Yasuhiko and K. Takeuchi, "In-silico clearing approach for deep refractive index tomography by partial reconstruction and wave-backpropagation," *Light Sci. Appl.* **12**, 101 (2023).
43. J. Scholler, K. Groux, O. Goureau, et al., "Dynamic full-field optical coherence tomography: 3D live-imaging of retinal organoids," *Light Sci. Appl.* **9**, 140 (2020).
44. T. Monfort, S. Azzollini, J. Brogard, et al., "Dynamic full-field optical coherence tomography module adapted to commercial microscopes allows longitudinal in vitro cell culture study," *Commun. Biol.* **6**, 992 (2023).
45. A. J. Walsh, R. S. Cook, M. E. Sanders, et al., "Quantitative optical imaging of primary tumor organoid metabolism predicts drug response in breast cancer," *Cancer Res.* **74**, 5184–5194 (2014).
46. D. Cappabianca, D. Pham, M. H. Forsberg, et al., "Metabolic priming of GD₂ TRAC-CAR T cells during manufacturing promotes memory phenotypes while enhancing persistence," *Mol. Ther. Methods Clin. Dev.* **32**, 101249 (2024).
47. K. P. Mueller, N. J. Piscopo, M. H. Forsberg, et al., "Production and characterization of virus-free, CRISPR-CAR T cells capable of inducing solid tumor regression," *J. ImmunoTher. Cancer* **10**, e004446 (2022).
48. P. C. Costa, P. Ledwig, A. Bergquist, et al., "Noninvasive white blood cell quantification in umbilical cord blood collection bags with quantitative oblique back-illumination microscopy," *Transfusion* **60**, 588–597 (2020).
49. T. Ford, K. Chu, and J. Mertz, "Phase-gradient microscopy in thick tissue with oblique back-illumination," *Nat. Methods* **9**, 1195–1197 (2012).
50. P. C. Costa, Z. Guang, P. Ledwig, et al., "Towards in-vivo label-free detection of brain tumor margins with epi-illumination tomographic quantitative phase imaging," *Biomed. Opt. Express* **12**, 1621–1634 (2021).
51. M. J. Saxton and K. Jacobson, "Single-particle tracking: applications to membrane dynamics," *Annu. Rev. Biophys. Biomol. Struct.* **26**, 373–399 (1997).
52. K. L. Fehrenbacher, H.-C. Yang, A. C. Gay, et al., "Live cell imaging of mitochondrial movement along actin cables in budding yeast," *Curr. Biol.* **14**, 1996–2004 (2004).
53. J. Sankaran, M. Manna, L. Guo, et al., "Diffusion, transport, and cell membrane organization investigated by imaging fluorescence cross-correlation spectroscopy," *Biophys. J.* **97**, 2630–2639 (2009).
54. G. I. Redford and R. M. Clegg, "Polar plot representation for frequency-domain analysis of fluorescence lifetimes," *J. Fluoresc.* **15**, 805–815 (2004).
55. F. E. Robles, J. W. Wilson, M. C. Fischer, et al., "Phasor analysis for non-linear pump-probe microscopy," *Opt. Express* **20**, 17082–17092 (2012).
56. R. M. Haralick, K. Shanmugam, and I. Dinstein, "Textural features for image classification," *IEEE Trans. Syst. Man Cybern. SMC-3*, 610–621 (1973).
57. A. F. Costa, G. Humpire-Mamani, and A. J. M. H. Traina, *An Efficient Algorithm for Fractal Analysis of Textures* (IEEE, 2012).
58. R. C. Gonzalez and R. E. Woods, *Digital Image Processing* (Pearson, 2012), Vol. 4.
59. F. E. Robles, J. Wilson, and W. Warren, "Quantifying melanin spatial distribution using pump-probe microscopy and a 2-D morphological auto-correlation transformation for melanoma diagnosis," *J. Biomed. Opt.* **18**, 120502 (2013).
60. F. E. Robles, S. Deb, J. W. Wilson, et al., "Pump-probe imaging of pigmented cutaneous melanoma primary lesions gives insight into metastatic potential," *Biomed. Opt. Express* **6**, 3631–3645 (2015).
61. S. L. Jacques, "Optical properties of biological tissues: a review," *Phys. Med. Biol.* **58**, R37–R61 (2013).
62. <https://biorender.com/>.